Iranian Journal of Geophysics, Vol 20 No 3, 2026, Page 1 – 24 (Research Article)
DOI: 10.30499/ijg.2026.569027.1746

Nonlinear Shear Behavior of Rock Joints and Stress Wave Propagation in Viscoelastic Sandstone

Alireza Nadi [1*], Reza Naghdabadi [2] and Kamran Goshtasbi [3]

[1] M.Sc., *Faculty of Engineering, Tarbiat Modares University, Tehran, Iran*
[2] *Professor, Sharif University of Technology, Tehran, Iran*
[3] *Professor, Faculty of Engineering, Tarbiat Modares University, Tehran, Iran*

(Received: 27 December 2025, Accepted: 13 April 2026)

Abstract
Studying the seismic response of rock mass has been in the limelight during recent decades. In the present study, the Kelvin-Voigt model is adopted to model rock material viscosity, where a nonlinear shear criterion is also employed to include the sliding mechanism across the joints. Both are then incorporated in the time-domain recursive method (TDRM) for calculating transmission and reflection coefficients. In order to assess the outcomes, a linearly elastic shear model is separately employed in the code so that the results can be comparatively analyzed. In the developed code, the dynamic shear stress of the joints is monitored at each time step with respect to the dynamic shear strength in a way that sliding occurs whenever the slipping criterion is satisfied over a range of quality factors. Results clearly show that slipping exerts a significant negative effect on the shear transmission coefficients while inducing the opposite on the reflection coefficients. It is also observed that joint spacing plays a dual role on the results, as emboldening the viscosity effects on one hand while improving the stability of the joints against sliding, on the other. This phenomenon, which is induced by the dynamic normal stress of the joints, is shown to be reduced to zero in the case of normal incidence angle, where the dynamic shear strength solely arises from the initial static shear strength. It is also shown that the maximum shear transmission coefficient could occur in a specific quality factor, wherein the sliding starts to happen.

Keywords: Stress Wave Propagation. Joint Slipping. Viscoelasticity. Transmission and Reflection Coefficients. Joint Spacing. Time-Recursive Method

*Corresponding author: a.nadi@modares.ac.ir

1 Introduction

A broad spectrum of rock engineering projects and rock structures are under the influence of dynamic loads generated by high-energy phenomena, including seismic events, rock-bursts, blasting operations and projectile penetrations. This range of disturbing events induces complex wave fields to propagate through jointed rock mass, leading to significant variations in stress, deformation and energy distribution. That is why understanding the mechanisms governing stress wave propagation and the associated energy dissipation is highly essential in the evaluation of stability and dynamic response of underground structures and rock engineering systems.

Most of the previous studies on stress-wave propagation through jointed rock masses have adopted simplified linear elastic models, especially in shear modes, to represent the mechanical behavior of rock joints (Chai et al. 2016, Li and Ma 2010, Schoenberg 1980, Zhao and Cai 2001). However, the shear-slip response of joints has been rarely incorporated in the complex sets of joints, despite its significant role under realistic loading conditions. In natural rock masses, joints are frequently subjected to dynamic loads exceeding the elastic limit, resulting in slip or inelastic deformation of rock joints. Previous theoretical and numerical studies have rarely addressed the reformation of transmitted and reflected waves resulted by slipping behavior of joints.

In recent studies, various analytical methods have been developed to investigate stress wave propagation through the jointed rock mass. Schoenberg (1980) employed the Displacement Discontinuity Method (DDM) to model the propagation and reflection of elastic waves across linear slip interfaces. Bedford and Drumheller (1994) used characteristic line theory to formulate one-dimensional equations of motion for elastic waves. Li and Ma (2010) adopted the time-domain recursive method (TDRM) to investigate the dynamic interaction between blast-induced stress waves and a rock joint, revealing that joint stiffness and incident wave amplitude play a crucial role in wave attenuation and energy dissipation of stress waves. Li and Ma (2011) Conducted a research on a single joint considering the slipping shear behavior of rock joints in elastic media and showed that the shear particle velocity of the joint is limited to a maximum value while slipping. Li and Ma (2012) developed and applied a time-domain recursive approach to model the propagation of transient stress waves across rock joints.

Li et al. (2018) modeled the rock fault as a Kelvin-Voigt viscoelastic medium and used a time-recursive analytical scheme to compute wave coefficients. Chai et al. (2017) employed the Kelvin model and demonstrated that an increase in viscosity leads to greater attenuation and lower wave amplitudes. Huang et al. (2014) developed the Propagator Matrix Method (PMM) to model wave transmission and reflection and showed that PMM efficiently predicts wave amplitude variations and phase shifts caused by joint stiffness and layer properties.

Nevertheless, none of the aforementioned studies have examined the influence of shear slipping of rock contact interfaces on both P-wave and S-wave transmission-reflection coefficients in a set of rock joints. Additionally, a few studies have recently addressed the combined effects of viscosity and slipping conditions on the wave coefficients. In low-porosity rocks, especially those with a clay-rich matrix, where the effect of pore-fluid pressure on the overall mechanical response is negligible, the degree of water saturation can still exert a significant influence on the stiffness of the rock frame. In such clay-bearing formations, increased saturation leads to softening of the clay minerals and increased inter-particle sliding. These combined effects can result in a substantial reduction in elastic stiffness and shear strength, along with a significant increase in effective viscosity and energy dissipation and consequently greater attenuation of seismic waves in saturated rock mass.

Several studies have experimentally demonstrated that water saturation degree is one of the most important factors that significantly control the viscoelasticity and attenuation coefficients of elastic waves in rock mass media (Hu, Wang 2022, Li, Wang 2022, Zheng and Zuo 2024, Best 1992). Huang et al. (2014) used PMM and showed that increased water saturation significantly enhances attenuation coefficients and reduces transmission amplitudes. Yang et al. (2024) experimentally concluded that increasing water content markedly reduces wave velocity and amplifies attenuation, highlighting the strong correlation of energy dissipation with moisture. Huang et al. (2020) employed the PMM technique and studied 2-D stress wave propagation through viscoelastic rock joints in different water contents and demonstrated that highly-saturated filling material has a significant effect on the quality factor, providing a substantial decrease in transmission coefficients of the incident stress wave.

In the present study, we firstly conducted several quasi-static experiments according to ISRM standards and additionally performed a meticulous mineralogical analysis on a type of low-porosity rock called Shemshak sandstone with a clay-rich matrix and recorded significant reductions in the mechanical parameters of fully saturated Shemshak sandstone with respect to air-dried samples. We consequently employed the Kelvin-Voigt model to represent the viscoelasticity of the saturated Shemshak sandstone in the analytical solutions. A nonlinear Coulomb shear slipping model is also adopted for a set of three rock joints to analytically investigate the transmission-reflection coefficients of an incident shear stress wave using the time-domain recursive analysis method (TDRM) and the results are subsequently compared with those from linearly-elastic shear behavior of the joints. The results of the current research can provide certain support to the analysis of stress wave attenuation in viscoelastic rock mass media in a jointed rock system and it can potentially improve the stability analysis of rock mass structures under dynamic loading conditions.

2 Quasi-Static Results

2.1 Mineralogical Composition Analysis

In the present study, Shemshak sandstone is collected from the surroundings of the Shemshak-to-Dizin road in the north of Tehran, Iran. The mineralogical analysis was conducted using polarized-light microscopy (PLM) to identify the mineral composition of the sandstone, as shown in Table 1. In addition, the amplified microscopic picture of a thin-section prepared from the sandstone is shown in Fig. 1.

Table 1 Mineral composition of Shemshak sandstone.

Minerals	Content (volume %)	Grain size (mm)
Quartz	50	0.25-0.626
Feldspar	20	0.25-0.626
Micas (Muscovite, Biotite, Sericite, Chlorite)	20	0.25-0.626
Chert, Dark Minerals	10	0.25-0.626

As shown in the table. 1, microscopic observations reveal that Shemshak sandstone contains about 50% of monocrystalline and polycrystalline quartz as well as 20% of alkali and plagioclase feldspar, characterized by distinct polysynthetic twinning within the sandstone. It also comprises 20% of minerals, including muscovite, sericite, chlorite and other clayey and micaceous minerals occupying the interstitial spaces between quartz and feldspar grains. Thus,

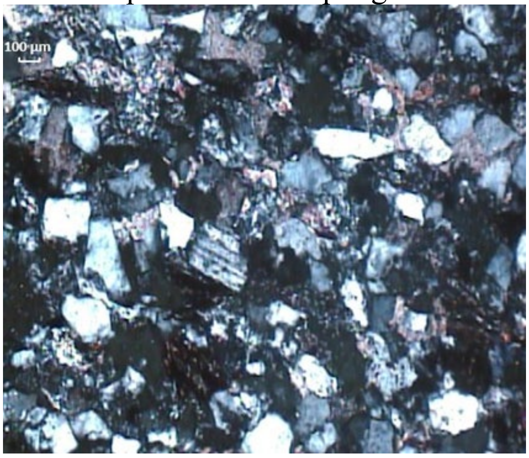

Fig. 1 Microscopic photo of Shemshak sandstone.

according to the petrographic Folk classification (Rocks 1968), Shemshak sandstone is a submature meta-sublitharenite sandstone containing more than 15% clay in the matrix and this is why it can be highly susceptible to water saturation in terms of rock mechanical parameters. Additionally, due to the clay-rich matrix of Shemshak sandstone, it could substantially acquire a significant level of viscosity in water-saturated conditions.

2.2 Laboratory tests

We conducted a series of well-known laboratory rock tests on Shemshak sandstone according to ISRM suggested methods in order to measure the mechanical parameters to take insights into the mechanical behavior of clay-rich Shemshak sandstone (Bieniawski and Bernede 1979, Chen, Pan 1998). The porosity of Shemshak sandstone is measured as low as 0.77%. In addition, the densities of air-dried and water-saturated samples are also measured as 2762 kg/m^3 and 2869 kg/m^3 for Shemshak sandstone. Moreover, we conducted a series of quasi-static tests including uniaxial and Brazilian tests in order to determine Young's modulus, compressive strength, Poisson's ratio and tensile strength of Shemshak sandstone, as shown in the table. 2.

It is obvious from Table 2 that clay-rich Shemshak sandstone is highly susceptible to water saturation as the uniaxial compressive strength, Young's modulus and tensile strength of Shemshak sandstone have remarkably reduced by 40%, 47% and 56%, respectively.

Table 2 Mechanical parameters of Shemshak sandstone.

Moisture state	Uniaxial compressive strength (MPa)	Young's modulus (GPa)	Poisson's ratio	Tensile strength (MPa)
Natural	159.13	39.63	0.17	11.58
Saturated	96.54	20.89	0.16	5

This range of reductions in rock mechanical parameters clearly demonstrates that clay-rich Shemshak sandstone is profoundly affected by water saturation and consequently, it is of utmost importance to take into account the effect of viscosity variations in studying stress wave propagation through jointed Shemshak sandstone media. Moreover, multiple ultrasonic tests were conducted and the P-wave speed in Shemshak sandstone in two air-dried and fully water-saturated conditions was obtained on average 4089 m/s and 2850 m/s, respectively. This reduction in P-wave speed is fairly plausible for such a clay-rich sandstone with very low porosity, which could be attributed to water softening of the rock (Yin, Borgomano 2019, Xu, Huang 2024). In other words, rock frame in saturation is substantially undermined through water absorption into the clayey matrix so that no subsequent enhancement is induced in the P-wave velocity as the rock porosity is extremely insignificant.

3 Solution Method

3.1. Problem description

3.1.1 Viscoelastic model

In the present study, we employ the Kelvin-Voigt viscoelastic model to implement the viscoelasticity of fully saturated clay-rich Shemshak sandstone in our analytical solution codes. Using stress-strain relation in isotropic media as shown in Eq. 1, the viscoelastic Kelvin-Voigt equation can be expressed according to the Principle of Correspondence as Eq.2 (Carcione 2007):

$$\sigma_{ij} = 2\mu\varepsilon_{ij} + \lambda\delta_{ij}\varepsilon_{kk} \tag{1}$$

$$\sigma = E\varepsilon + \eta\dot{\varepsilon} = \left(\lambda\theta + \lambda'\dot{\theta}\right)\delta_{ij} + 2\mu\varepsilon_{ij} + 2\mu'\dot{\varepsilon}_{ij} \tag{2}$$

According to the solution to the one-dimensional wave field equation in elastic media, as shown in Eq. 3, the viscoelastic Kelvin equation is summarized in Eq. 4 (Carcione, Poletto 2004):

$$u(x,t) = Ae^{i(K_\omega x \pm \omega t)} \tag{3}$$

$$\sigma_{ij} = \Lambda\theta\delta_{ij} + 2\Sigma\varepsilon_i \qquad (\Lambda = \lambda + i\omega\lambda' \,.\, \Sigma = \mu + i\omega\mu') \tag{4}$$

By definition of attenuation coefficient α for a stress wave as the imaginary part of the complex frequency-dependent wave number K_ω in Eq. 3, and substituting it into the complex quality factor equation as demonstrated in Eq. 5, the quality factor, the attenuation coefficients as well as the real parts of complex wave numbers for both P and S waves can be separately represented as Eqs. 6-9 (Carcione, Poletto 2004):

$$Q = -\frac{Re(K_\omega^2)}{Im(K_\omega^2)} \tag{5}$$

$$\alpha_p^2 = \frac{\rho\omega^2}{2E(1+\frac{1}{Q_p^2})}\left(\sqrt{1+\frac{1}{Q_p^2}} - 1\right) \tag{6}$$

$$k_{real}^2(p) = \frac{\rho\omega^2}{2E\left(1+\frac{1}{Q_p^2}\right)}\left(\sqrt{1+\frac{1}{Q_p^2}} + 1\right) \tag{7}$$

$$\alpha_s^2 = \frac{\rho\omega^2}{2\mu(1+\frac{1}{Q_s^2})}\left(\sqrt{1+\frac{1}{Q_s^2}} - 1\right) \tag{8}$$

$$k_{real}^2(s) = \frac{\rho\omega^2}{2\mu\left(1+\frac{1}{Q_s^2}\right)}\left(\sqrt{1+\frac{1}{Q_s^2}} + 1\right) \tag{9}$$

Where ρ is the density of the media, ω is the wave angular frequency, E and μ are the stiffness modulus of the media, α_p and α_s are attenuation coefficients for P and S waves, Q_p and Q_s are quality factors of the rock media for P-wave and S-wave, respectively. Subsequently, the harmonic solution to the 1-D wave equation for viscoelastic media can be rewritten as shown in Eq. 10.

$$u(x,t) = Ae^{-\alpha x}e^{i(K_{real}x \pm \omega t)} \tag{10}$$

3.1.2 Time-domain recursive method

According to the field equations of one-dimensional stress wave propagation, when an incident P-wave or S-wave impinges obliquely on the left side of the first joint as shown in Fig. 2, the reflection and transmission of both P and S waves occur through the shear and normal behavior of the rock joint so that the angles of incident, reflected and transmitted P and S waves are the same for each case and are α and β, respectively.

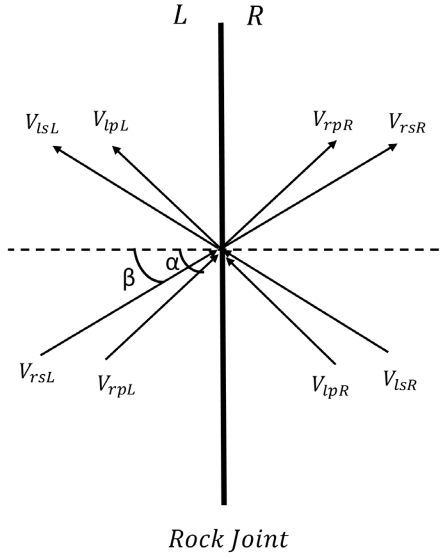

Fig. 2 Transmission and Reflection of Waves at Joint Interface.

As shown in Fig. 2, the first letter in the subscript of each particle velocity represents the direction of wave propagation, the second one indicates the type of wave and the third denotes whether the wave interacts with the left side or right side of the joint interface. Thus, for example, V_{lsl} refers to the particle velocity of a left-running S-wave reflecting from the left side of the joint, while V_{rpr} indicates the particle velocity of a right-running P-wave transmitting from the right side of the joint.
The relationship between the angles α and β in terms of Poisson's ratio ϑ of media is determined by Snell's Law according to Eq. 10.

$$\sin\alpha/\sin\beta = C_p/C_s = \sqrt{2(1-\vartheta)/(1-2\vartheta)} \tag{10}$$

In order to study stress wave propagation in water-saturated Shemshak sandstone media, we firstly assume a set of three non-welded parallel rock joints which are planar, large in extent and small in thickness compared to the wavelength, lying in the x-y plane and extending to infinity, as shown in Fig. 3. Additionally, the rock material is assumed to be homogeneous and isotropic everywhere. Moreover, there are secondary incident P and S waves on the sides of the joints because of multiple reflections between every two adjacent joints.

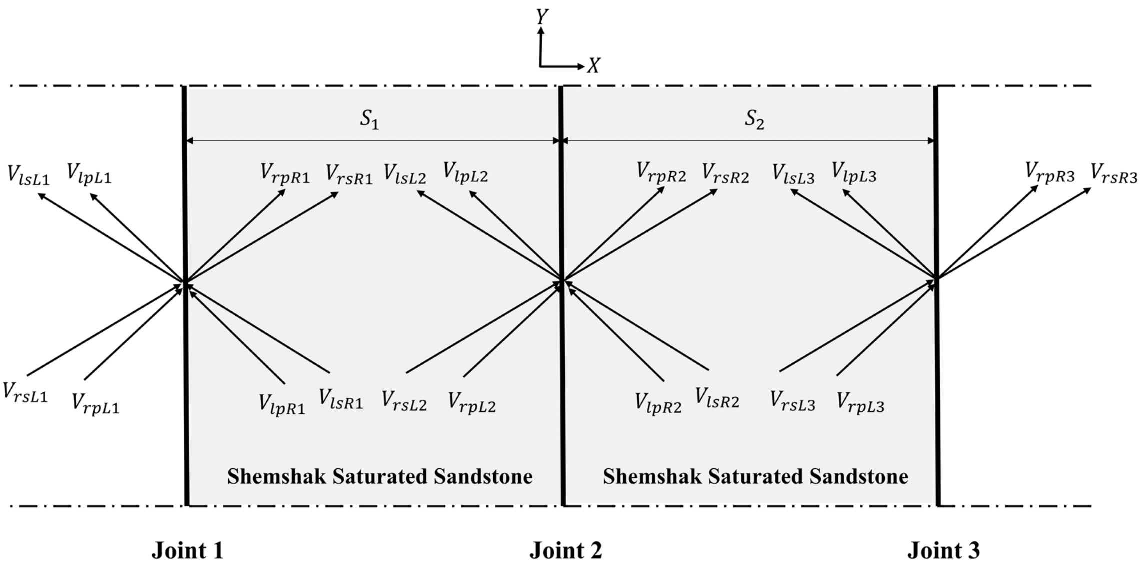

Fig. 3. Transmission and Reflection of Waves at Interfaces for Three Joints.

Figs. 4 and 5 demonstrate the total shear and normal stresses on the two sides of each joint resulting from the potential stress waves according to Fig. 3. In the present study, the rock media is considered as plain strain media while the incident wave is considered one-dimensional and the body forces are not accounted for in the equations.

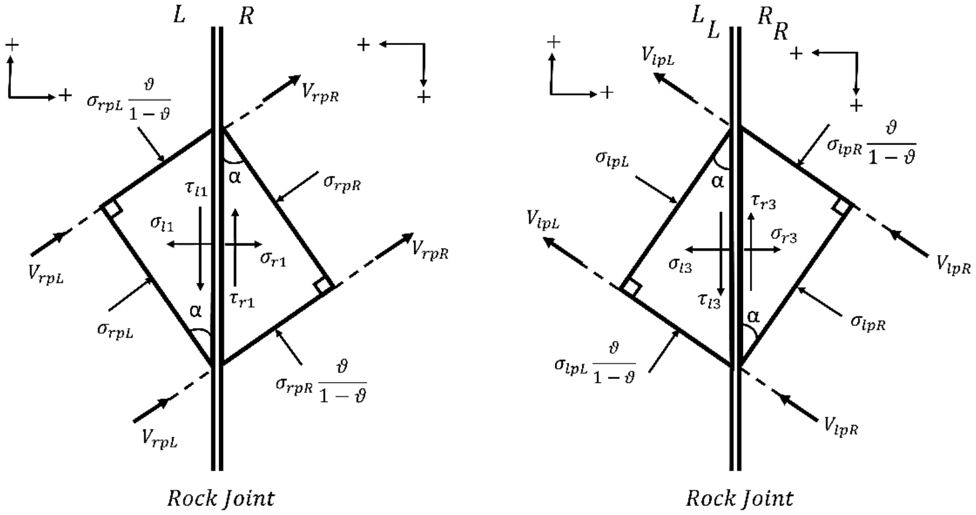

Fig. 4. Total shear and normal stresses on both sides of the joint induced by normal stress waves.

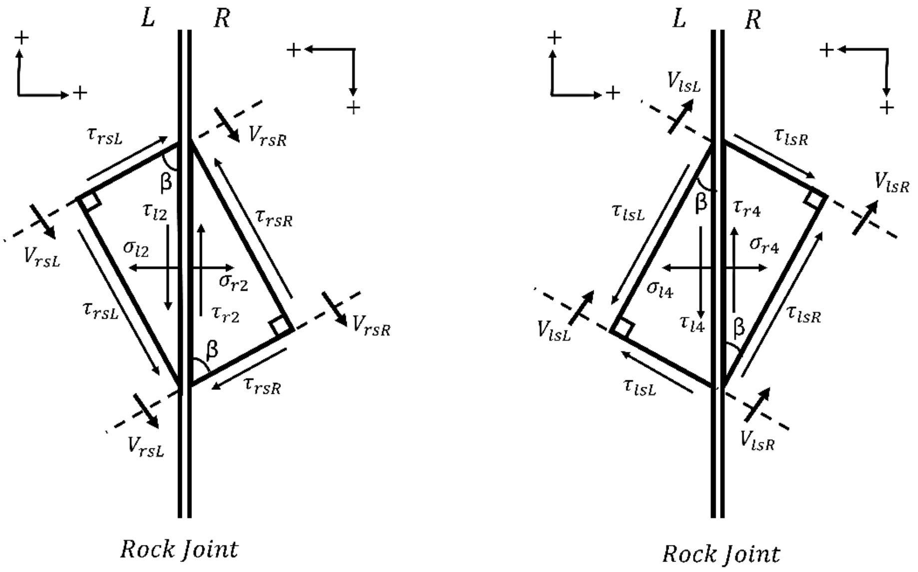

Fig. 5. Total shear and normal stresses on both sides of the joint induced by shear stress waves.

According to the stress continuity for each joint, the total shear and normal stresses at both sides of the joint should be equal, as shown in Eq. 11:

$$\sigma_L = \sigma_R \,. \quad \tau_L = \tau_R \tag{11}$$

Where the letters L and R represent the left and right sides of the joint, respectively. In addition, and based on the conservation of a, the relationship of stresses and particle velocities for both normal and shear components can be described as Eq. 12:

$$\sigma = z_p V_p \,. \quad \tau = z_s V_s \tag{12}$$

Where z_p and z_s are impedances for P and S waves, respectively and are obtained based on the density and the phase velocities of the wave in the rock media, as $z_p = \rho C_p$ and $z_s = \rho C_s$. By establishing equilibrium equations for each triangle element in Figs. 4 and 5 and using Eq. 12, we can obtain the total shear and normal stresses on each side of each joint as shown in Eqs. 13-16:

$$\sigma_L = \sigma_{l1} + \sigma_{l2} + \sigma_{l3} + \sigma_{l4} = a_1 V_{rpL} + a_2 V_{rsL} + a_3 V_{lpL} + a_4 V_{lsL} \tag{13}$$

$$\tau_L = \tau_{l1} + \tau_{l2} + \tau_{l3} + \tau_{l4} = b_1 V_{rpL} + b_2 V_{rsL} + b_3 V_{lpL} + b_4 V_{lsL} \tag{14}$$

$$\sigma_R = \sigma_{r1} + \sigma_{r2} + \sigma_{r3} + \sigma_{r4} = a_1 V_{rpR} + a_2 V_{rsR} + a_3 V_{lpR} + a_4 V_{lsR} \tag{15}$$

$$\tau_R = \tau_{r1} + \tau_{r2} + \tau_{r3} + \tau_{r4} = b_1 V_{rpR} + b_2 V_{rsR} + b_3 V_{lpR} + b_4 V_{lsR} \tag{16}$$

Where $a_1 - a_4$ and $b_1 - b_4$ are constants and are represented as Eqs. 17 and 18:

$$a_1 = a_3 = z_p \cos 2\beta \quad . \quad a_2 = -a_4 = z_s \sin 2\beta \tag{17}$$

$$b_1 = -b_3 = z_p \, sin\, 2\beta \, tan\, \beta / tan\, \alpha \quad . \quad b_2 = b_4 = -z_s \cos 2\beta \tag{18}$$

According to the directions of waves' particle motions as shown in Figs. 4 and 5, the total normal and shear particle velocities (V_n and V_s) at the left and right sides of each joint can also be calculated as Eqs. 19-22, respectively:

$$V_{nL} = \cos\alpha\, V_{rpL} + \sin\beta\, V_{rsL} - \cos\alpha\, V_{lpL} + \sin\beta\, V_{lsL} \tag{19}$$

$$V_{\tau L} = \sin\alpha\, V_{rpL} - \cos\beta\, V_{rsL} + \sin\alpha\, V_{lpL} + \cos\beta\, V_{lsL} \tag{20}$$

$$V_{nR} = \cos\alpha\, V_{rpR} + \sin\beta\, V_{rsR} - \cos\alpha\, V_{lpR} + \sin\beta\, V_{lsR} \tag{21}$$

$$V_{\tau R} = \sin\alpha\, V_{rpR} - \cos\beta\, V_{rsR} + \sin\alpha\, V_{lpR} + \cos\beta\, V_{lsR} \tag{22}$$

Based on the displacement discontinuity model and assuming a linearly elastic normal behavior and a nonlinear slipping shear Coulomb model for the rock joint, the relationship between the total normal and shear particle velocities at the sides of the joint can be expressed as Eqs. 23 and 24:

$$\sigma_{i+1} = \sigma_i + k_n \Delta t [V_{pL}(i) - V_{pR}(i)] \tag{23}$$

$$\begin{cases} \tau_{i+1} = \tau_i + k_s \Delta t [V_{sL}(i) - V_{sR}(i)] \\ \tau_{i+1} = \tau_i. \end{cases} \tag{24}$$

Where Δt is the adopted time step in the recursive method, i and $i+1$ are the two consecutive time steps and k_n, k_s are the normal and shear stiffness of the rock joint, respectively. By substituting Eqs. 13-16 and 19-22 at time step i into Eqs. 23 and 24, we can obtain the normal and shear particle velocities of the transmitted and reflected waves based on any incident particle velocity at each time step. It should be noted that for the problem of three parallel joints as depicted in Fig. 3, the only known incident particle velocities are V_{rpL1} and V_{rsL1} so that the other incident particle velocities are caused by multiple reflections in the spaces between the joints. These types of secondary incident waves are subject to the viscoelasticity as represented in Eq. 10 and can be obtained at each time step according to the joint spacing, speeds of P and S waves in the media and the angle of directions α and β for P and S waves, respectively. Considering Eqs. 6-10 in section 3.1.1, the secondary incident waves caused by multiple reflections can be calculated as Eq. 25-28:

$$V_{lpR1} = e^{(-\alpha_p S/\cos\alpha)} V_{lpL2}(i - n_p - n_{kp}) \tag{25}$$

$$V_{lsR1} = e^{(-\alpha_s S/\cos\beta)} V_{lsL2}(i - n_s - n_{ks}) \tag{26}$$

$$V_{rpL2} = e^{(-\alpha_p S/\cos\alpha)} V_{rpR1}(i - n_p - n_{kp}) \tag{27}$$

$$V_{rsL2} = e^{(-\alpha_s S/\cos\beta)} V_{rsR1}(i - n_s - n_{ks}) \tag{28}$$

Where α_p and α_s are attenuation coefficients of the rock media, respectively, n_p and n_s is the number of time steps needed for the P and S waves to travel the spacing joint S, and n_{kp} and n_{ks} There is also the time delay of P and S waves induced by the viscoelasticity of rock material between the joints and are calculated as Eqs. 29-31:

$$n_p = int[S/C_p \Delta t \cos\alpha]. \quad n_s = int[S/C_s \Delta t \cos\beta] \quad (29)$$

$$n_{kp} = int[S(k_p - k_{real}(p))/\omega dt]. = int[S(k_s - k_{real}(s))/\omega dt] \quad (30)$$

where $int[\,]$ represents the integer function, dt is the time step, ω wave angular frequency, C_p and C_p are the P and S phase velocities in the rock media, k_p, k_s are the wave numbers of the P and S waves at $Q_p = \infty$ and $Q_s = \infty$, and $k_{real}(p)$, $k_{real}(s)$ are the real parts of the complex wave numbers for P and S waves in viscoelastic rock media, respectively.

Ultimately, the transmission and reflection coefficients are quantitatively determined from the amplitude ratios of the transmitted waves emerging from joint 3 and the reflected waves originating from joint 1, with respect to the initial incident wave amplitude at joint 1, as represented in Eq. 31:

$$T_m = \frac{\max|V_{rmR3|}}{\max|V_{rmL1|}}. \quad R_m = \frac{\max|V_{lmL1|}}{\max|V_{rmL1|}} \quad (29)$$

Where m represents P and S waves, and in addition, T and R are the reflection and transmission coefficients in the present study.

4 Analytical Results and Discussion

4.1 Initial and Boundary Conditions

In the present study, an initial full-cycle sinusoidal incident shear stress wave (V_{rsL1}) is considered as Eq. 30, impinging obliquely on the left side of the joint 1 as depicted in Fig. 3, with the incident angle of β. The frequency f is considered 100 Hz, k_n and k_s of all the three joints are considered to be 2.5 GPa, joint spacing $S_1 = S_2$ and equal to 2.85 m, wave amplitude 1 m/s, wave period T as 0.01 s, $\beta = 20°$, and other physical parameters of Shemshak sandstone according to the data discussed in Section 2.1. Moreover, Q_p For saturated Shemshak sandstone is assumed to be $2Q_s$ for all cases. For the solution of the time recursive method, VBA Excel was used with a time step equal to $1/800f$ for computational efficiency and the accuracy of the results. In addition, a linearly elastic normal behavior is considered for the three rock joints, the shear behavior is set to be a linearly elastic shear model and a nonlinear Coulomb shear model in two different cases, as shown in Fig. 6.

$$V_{rsL1} = \begin{cases} -\sin(\omega t) & 0 \le t \le T \\ 0 & t > T \end{cases} \quad (30)$$

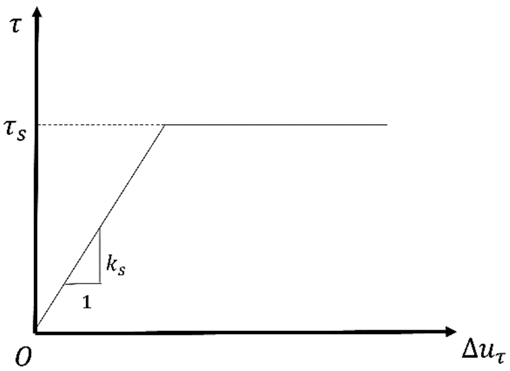

Fig. 6: Nonlinear shear Coulomb model adopted for the rock joints in the three-joint system.

4.1.1 viscoelastic saturated Shemshak Sandstone with linearly elastic shear behavior

Considering that the problem in the present study is based on shear incident stress wave, and given the high vulnerability of the sandstone's physical parameters to water saturation as illustrated in section 2.1, it is best to analyze the analytical results in the range 2.5-50 for the quality factor. The lowest range is set 2.5 as it is meaningless and impossible to assign infinity viscosity to the rocks. Plus, the highest range of quality factor is considered 100 as data sensitivity fades away at the lowest ranges of viscosity. Figs. 6 and 7 demonstrate the final transmitted and reflected P and S stress waves for the three-joint system in two different cases of Qs = 2.5 and Qs = 50. In addition, the variations of dynamic shear stress in joint 1 and the dynamic transmitted shear stress in joint 3 are shown in Figs. 9 and 10.

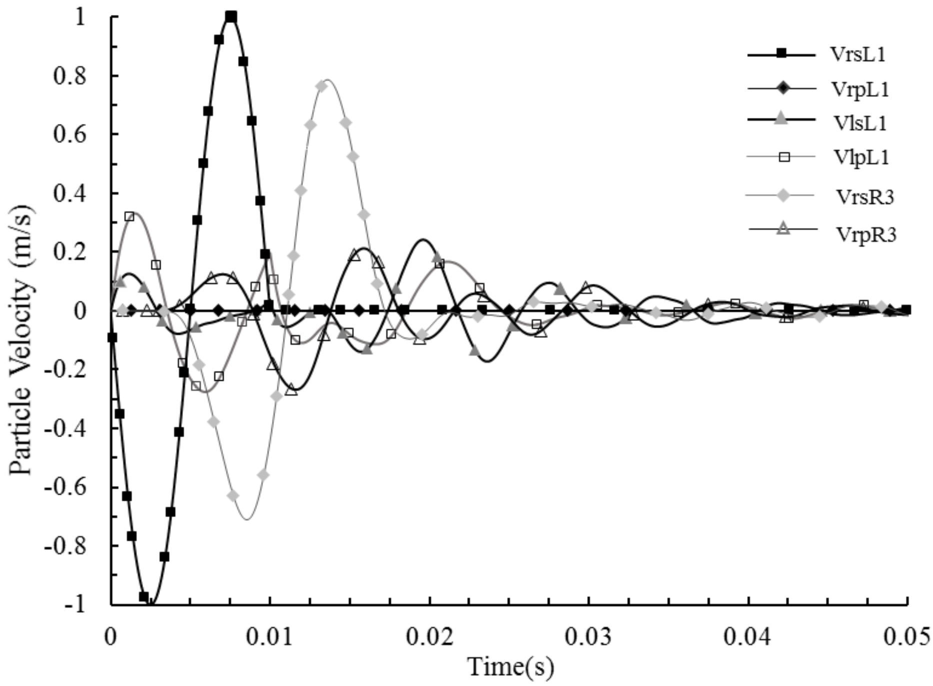

Fig. 7. The incident, reflected and transmitted waves system at $Q_s = 50$ (linearly elastic shear model).

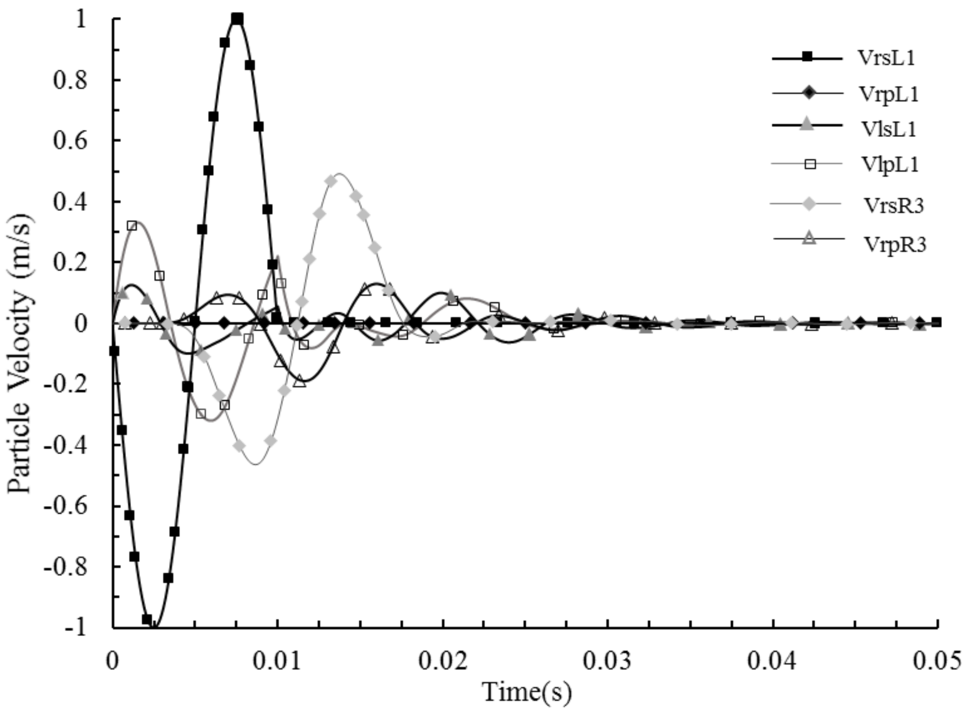

Fig. 8. The incident, reflected and transmitted waves at $Q_s = 2.5$ (linearly elastic shear model).

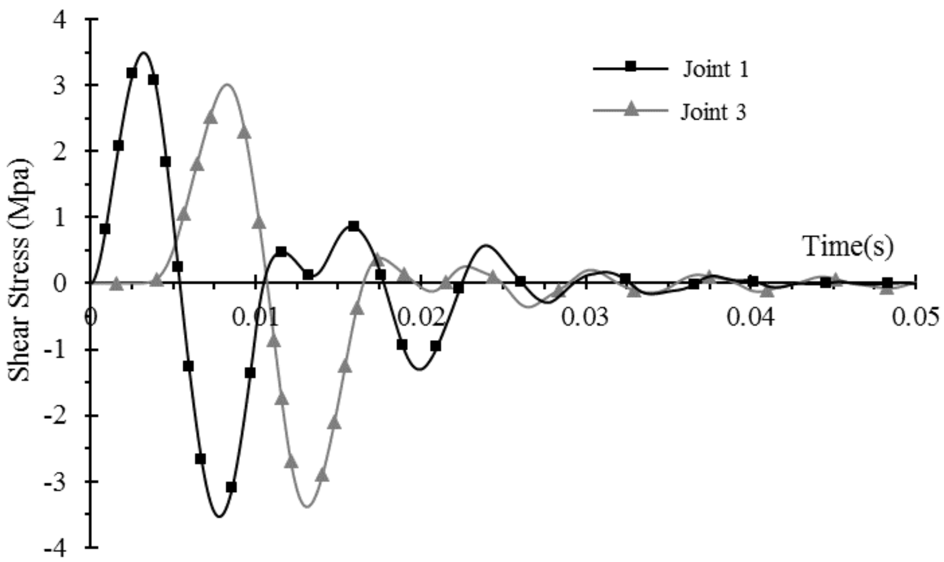

Fig. 9. Shear stresses for joints 1 and 3 at $Q_s = 50$ (linearly elastic shear model).

It is evident from the figures that the viscoelasticity of Shemshak sandstone induces a time delay on the phase velocities, as demonstrated by t_1 and t_2 in the charts. However, the time delay effect of viscoelasticity is not very significant in this case due to the relatively small propagation path of the waves in the space between the joints. Figs. 8 and 9 also represent the variations of the shear stress in joint 1 with respect to that in joint 3 over time.

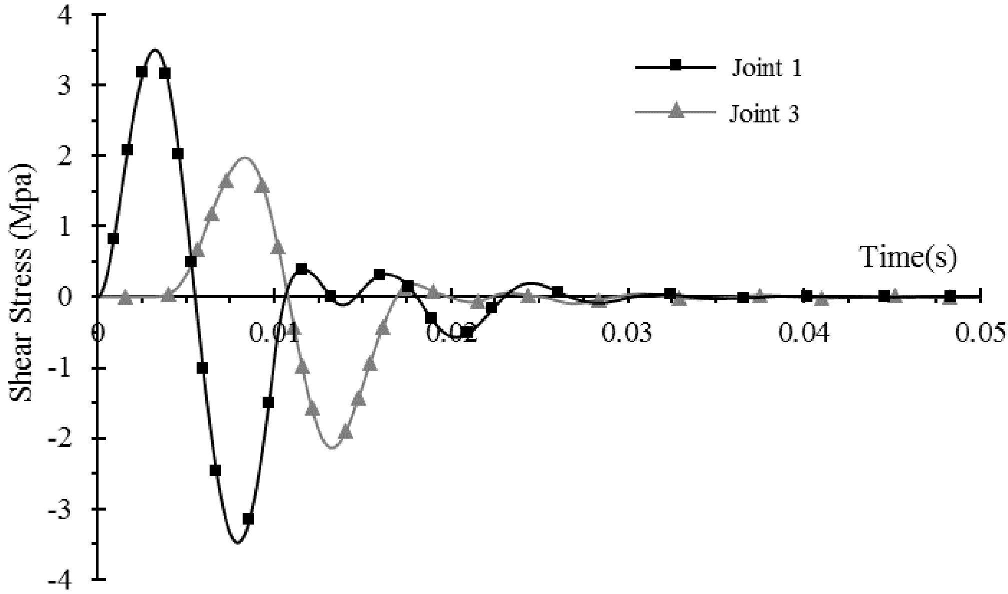

Fig. 10. Shear stresses for joints 1 and 3 at Q_s= 2.5 (linearly elastic shear model).

To investigate the time delay effect of media viscosity on the phase velocity, Fig. 11 shows the shear transmitted waves of the three-joint system in four different cases, where A and B indicate the joint spacing. $S_1 = S_2$ with both equaling to 2.85 m, while cases C and D correspond to the joint spacing $S_2 = 10S_1$ with S_1 equaling to 2.85m. In addition, cases A and C denote the quality factor as Qs = 50 while cases B and D represent Qs = 2.5. It could be obviously inferred from Fig. 11 that Δt_1 demonstrates the time delay due to the difference in the stress wave propagation paths for the two cases of $S_1 = S_2$ and $S_2 = 10S_1$, while Δt_2 represents the time delay due to the media viscosity for the case of $S_2 = 10S_1$ When the media quality factor changes from 50 to 2.5.

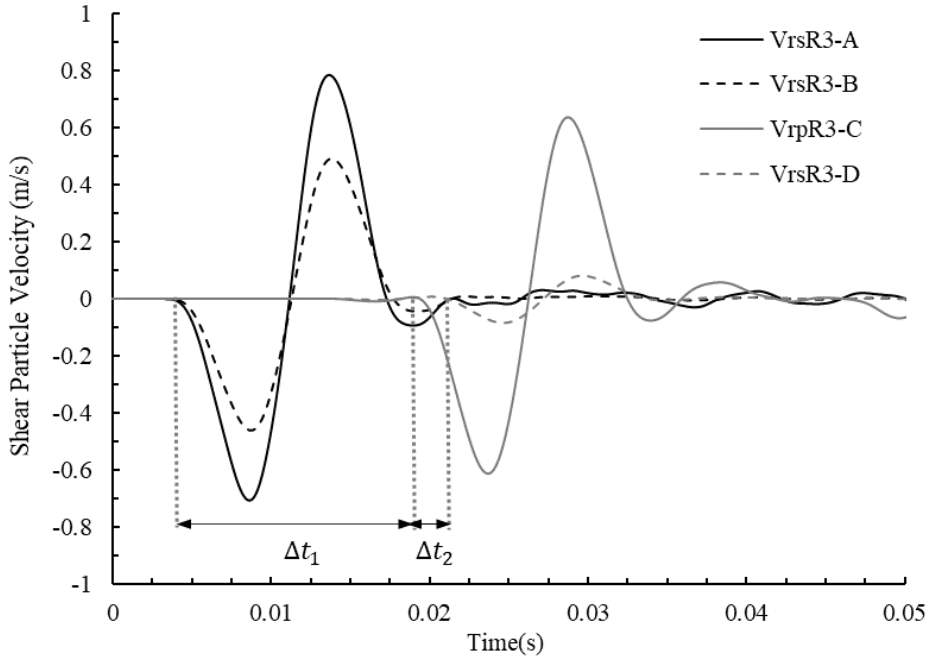

Fig. 11. Time delay effect by stress wave propagation path and media viscosity (linearly elastic shear model).

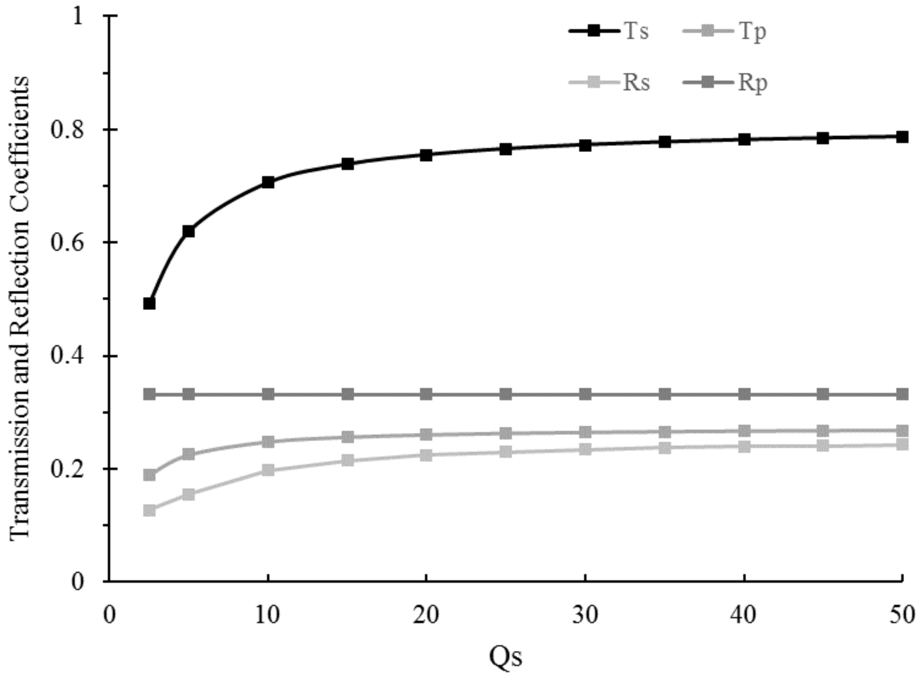

Fig. 12. Transmission and reflection coefficients with respect to viscosity (linearly elastic shear model).

In order to achieve a deeper and precise understanding of the influence of rock viscosity through the variation of quality factor values, the reflection and transmission coefficients of the three-joint system of the present study were calculated and examined for different Qs values, as illustrated in Fig. 12.

As shown in Fig. 12, the results indicate that in the three-joint system, with the change in the viscosity of Shemshak sandstone, the shear transmission coefficient, i.e. Ts, has most significantly changed by as much as 60% over the range of 2.5-50 for quality factor. More importantly, it is evident that the most significant changes in Fig. 12 are with respect to the shear transmission coefficient Ts which is essentially expected due to the shear nature of the incident stress wave in the present study. In contrast, the reflection coefficients of both P and S waves remain almost constant across all Qs values, so that the insignificant variations in the values of Rp and Rs arise only from the multiple reflections of the waves in the space between the joints.

4.1.2 viscoelastic saturated Shameshak Sandstone with nonlinear shear behavior

In this section, slipping is incorporated into the shear behavior of the three joints according to the Coulomb model as illustrated in Fig. 6. For that, the solution procedure requires at each time step to both calculate the instantaneous dynamic shear stress induced in the joint, i.e. $\tau(i)$, as well as the instantaneous dynamic shear strength of the joint, i.e. $\tau_s(i)$. To do that, the algorithm employs the Coulomb shear criterion as $\tau_s(i) = \tau_0 + \sigma(i)\tan\varphi$, in which σ is the dynamic normal stress on the joint, τ_0 is the initial static shear strength at the joint and φ is the internal friction angle. By comparing the values of $\tau(i)$ and $\tau_s(i)$, The TDRM solution code of the present study is updated at each time step according to Eq. 24 in section 3.1.2. If the dynamic shear stress in the joint exceeds the dynamic shear strength, slipping occurs across the joint and it continues until the joint is relaxed and re-enters the linear-elastic part. In order to perform the procedure in the present study, τ_0 and φ are assumed to be $z_s/7$ and 30°, respectively.

In order to validate the accuracy and reliability of the method used in the present study, the quality factor of the single-jointed rock media is set to infinity, with other parameters just the same as those used by Li et al. 2011 (Li, Ma 2011). Fig. 13 shows the results derived in normal incidence with the nonlinear shear model, compared to those obtained in the referenced research. It is clearly shown in Fig. 13 that the results are perfectly matched and consistent, meaning that the method derived in the present study is accurate and reliable.

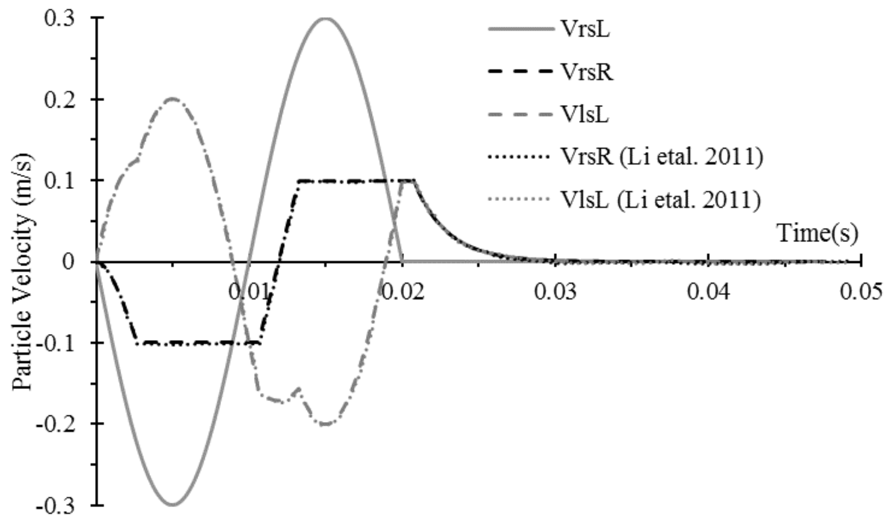

Fig. 13. Validation of the waves derived in the present study with respect to the reference paper.

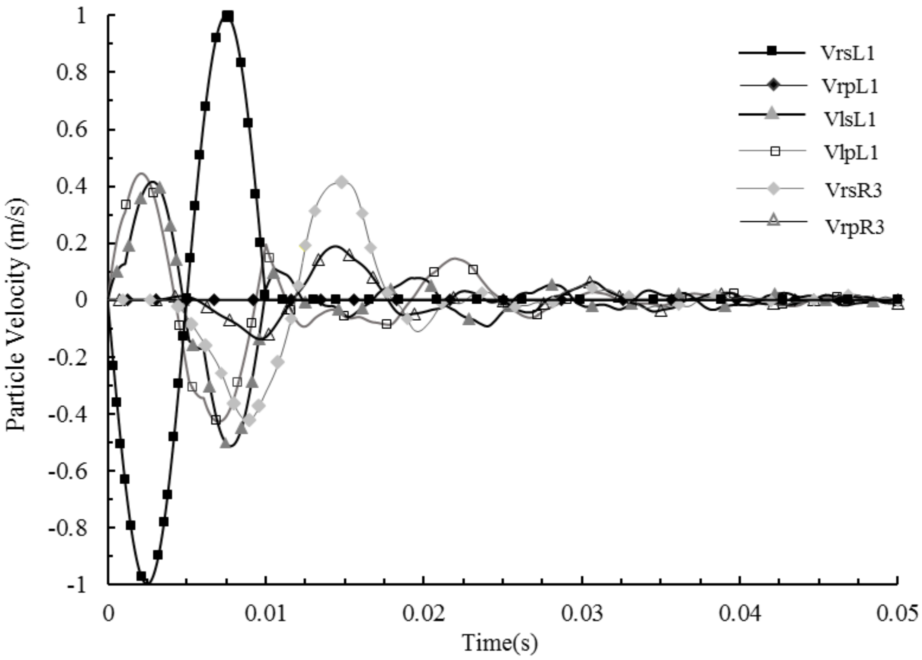

Fig. 14. The incident, reflected and transmitted waves at $Q_s = 50$ (nonlinear shear model).

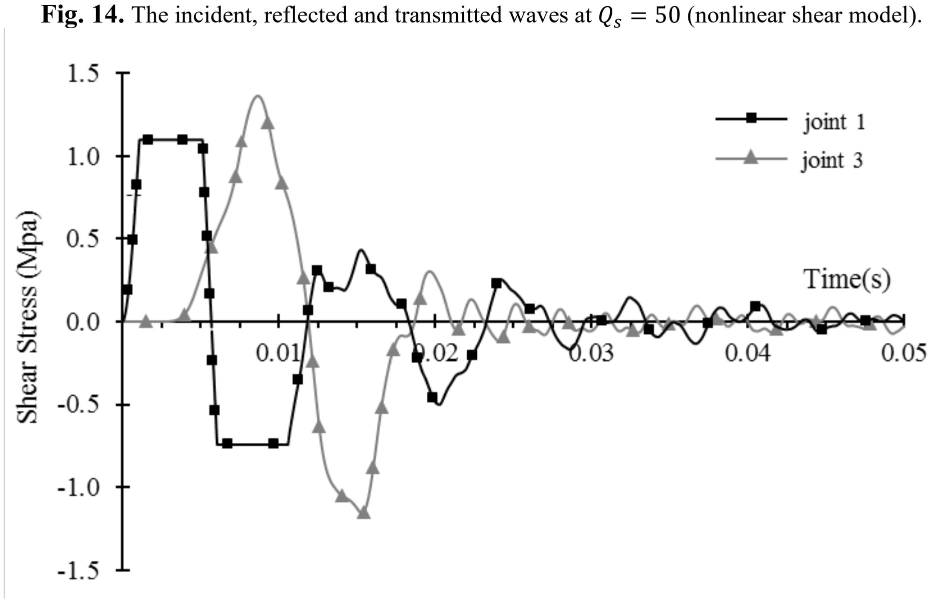

Fig. 15. Shear stresses for joints 1 and 3 at $Q_s = 50$ (nonlinear shear model).

Fig. 14 shows the incident, reflected and transmitted waves across the three-joint system at Qs = 50 for the nonlinear shear model. Comparing Figs. 14 and 7 clearly indicates the significant influence of nonlinear shear behavior of rock joints on stress wave propagation, as the maximum value of the transmitted shear particle velocity has substantially decreased compared to the linearly elastic shear model. This remarkable effect could be also identified through Fig. 14, where the peak of dynamic shear stress in the joint 3 has remarkably reduced compared to that in Fig. 9. It is also clear from Fig. 14 that joint 1 has slipped majorly in two different time periods so that the peak value for the dynamic shear stress is limited by the dynamic shear strength of the joint, i.e. $\pm\tau_{s1}(i)$, according to Coulomb shear criterion.

For verifying the efficiency of the shear model in the current study, Fig. 16 demonstrates how the instantaneous shear strength of the joint has restrained the dynamic shear stress over time.

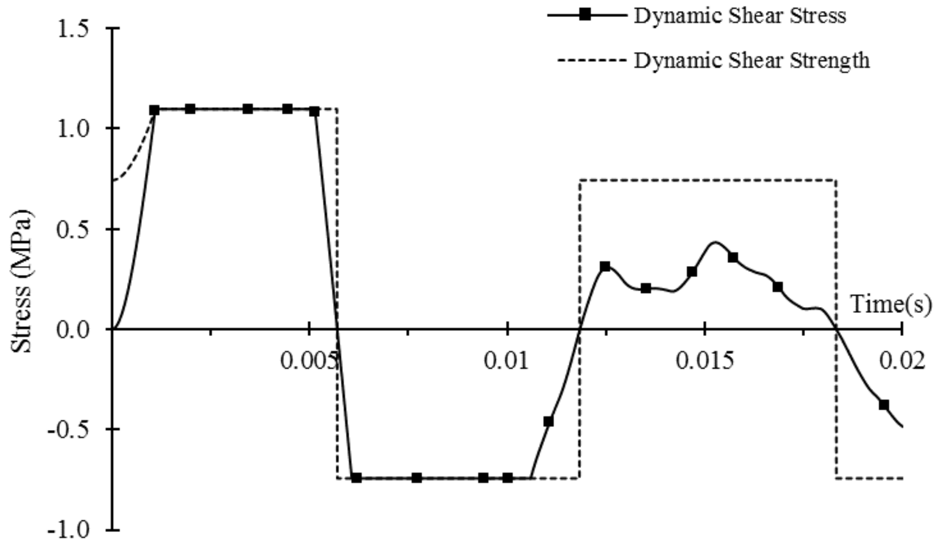

Fig. 16. Dynamic shear stress and strength for joint 1 at $Q_s = 50$ (nonlinear shear model).

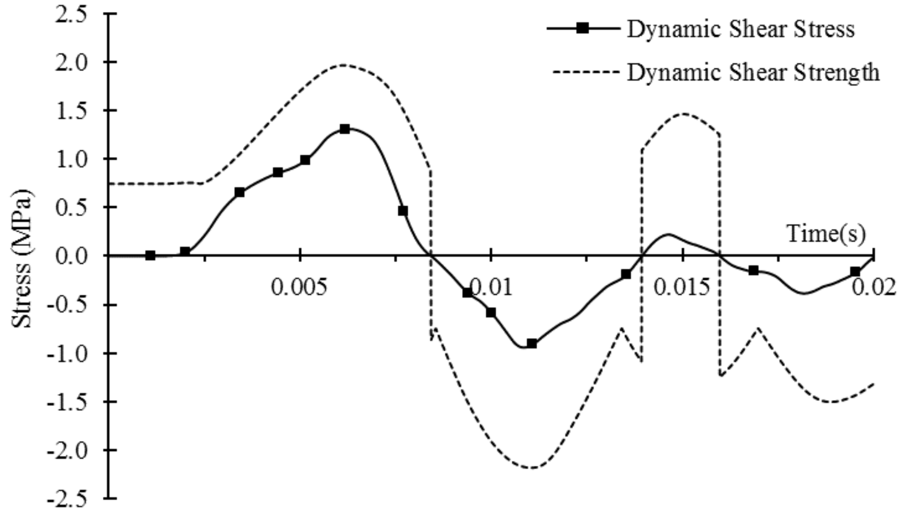

Fig. 17. Dynamic shear stress and strength for joint 2 at $Q_s = 50$ (nonlinear shear model).

In order to investigate whether slipping has also occurred for joints 2 and 3, Figs. 17 and 18 illustrate the variations of the dynamic shear stress and the dynamic shear strength at Qs = 50 for joints 2 and 3, respectively. It is obvious from the figures that slipping has not occurred for neither joint 2 nor joint 3. It is also obvious from Figs. 16-18 that the minimum of the dynamic shear strength for all joints before and after slipping is limited to the initial static shear strength of the joints, i.e., $\pm\tau_0$, so that the shift between τ_0 and $-\tau_0$ is instantaneous.

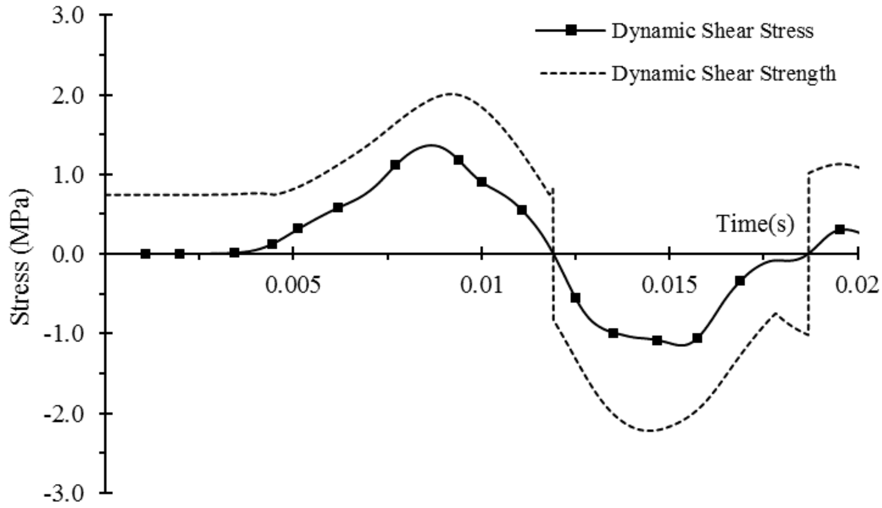

Fig. 18. Dynamic shear stress and strength for joint 3 at $Q_s = 50$ (nonlinear shear model).

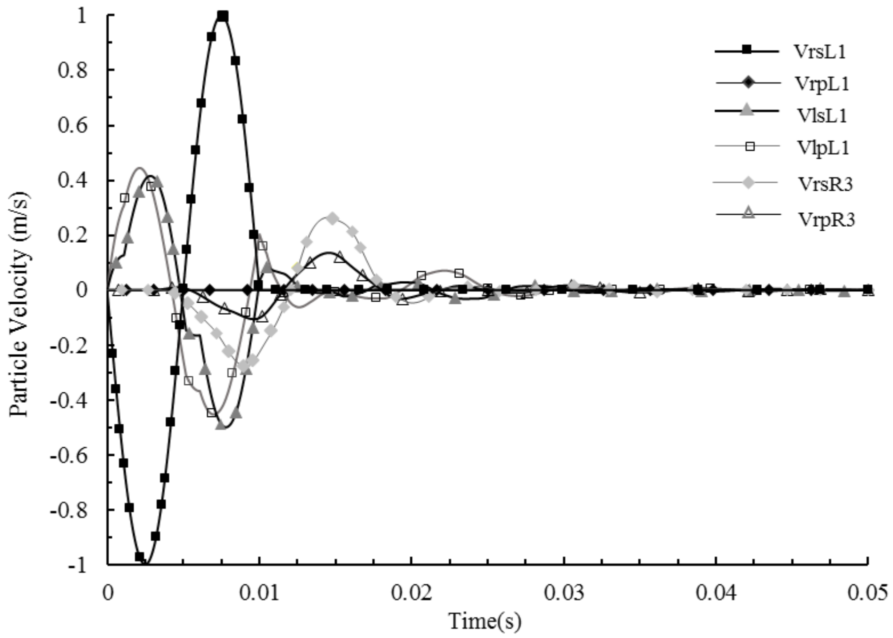

Fig. 19. The incident, reflected and transmitted waves at $Q_s = 2.5$ (nonlinear shear model).

In order to analyze the viscosity effect of Shemshak sandstone media for the nonlinear shear model, Figs. 19 and 20 represent the transmitted and reflected waves of the three-joint system at Qs = 2.5. It is clearly obvious from the figures that the amplitude of the transmitted shear particle velocity as well as the peak of the shear stress in joint 3 have decreased compared to those in Figs. 14 and 15. Moreover, the time delay for phase velocities at Qs = 2.5 with respect to Qs = 50 is almost insignificant due to the small wave propagation path, which is the same joint spacing.

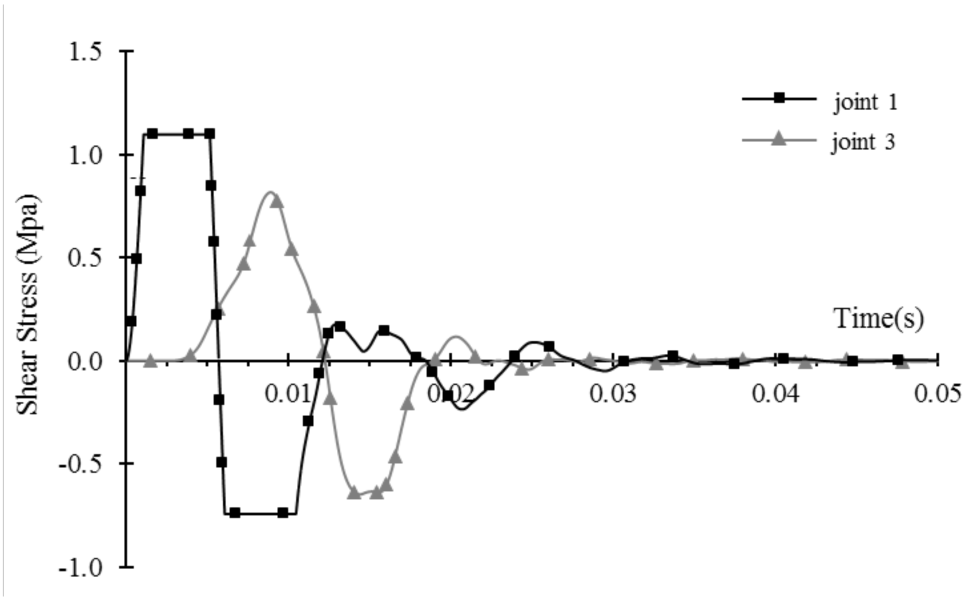

Fig. 20 Shear stresses for joints 1 and 3 at $Q_s = 2.5$ (nonlinear shear model).

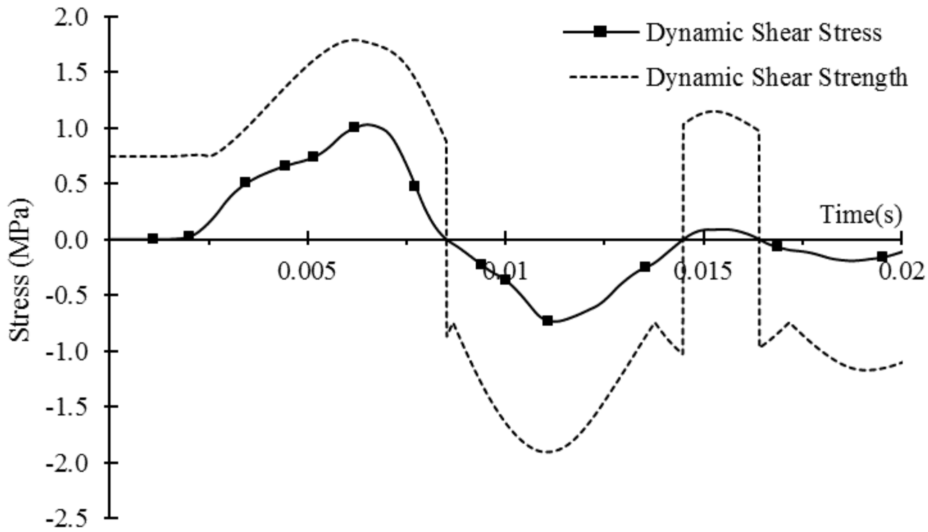

Fig. 21. Dynamic shear stress and strength for joint 2 at $Q_s = 2.5$ (nonlinear shear model).

It is also clear from Fig. 20 that slipping has similarly occurred for joint 1, but the peak of the dynamic shear stress in joint 3 has substantially decreased compared to that in Fig. 15. Moreover, the oscillations in the graphs, which are caused by multiple reflections or the same secondary incident waves, have been significantly attenuated at $Q_s = 2.5$.

Figs. 21-22 show the variations in the dynamic shear stress and strength of the joints 2 and 3 at $Q_s = 2.5$, respectively. It is evident that, similar to the case $Q_s = 50$, neither of joints 2 or 3 has experienced sliding, with a greater divergence between the dynamic shear stress and strength, as compared to Figs. 17 and 18.

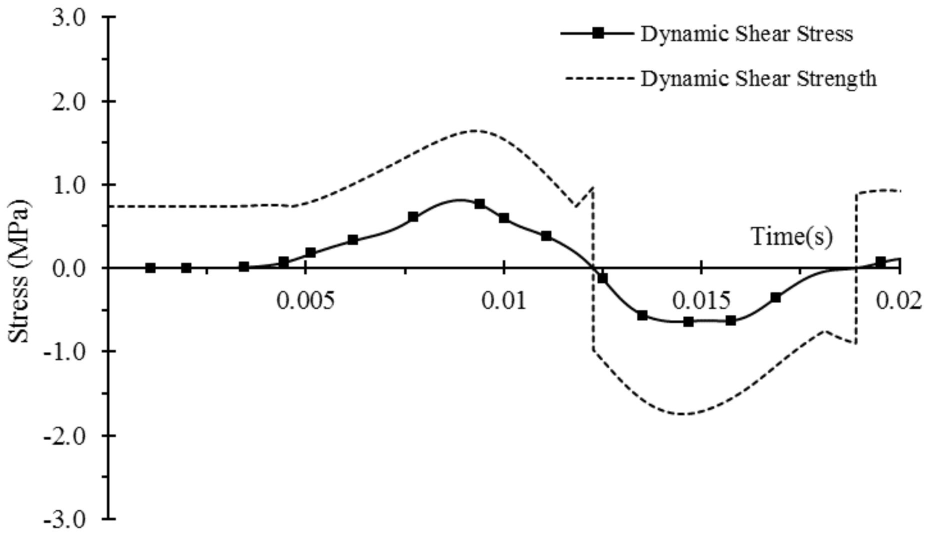

Fig. 22. Dynamic shear stress and strength for joint 3 at $Q_s = 2.5$ (nonlinear shear model).

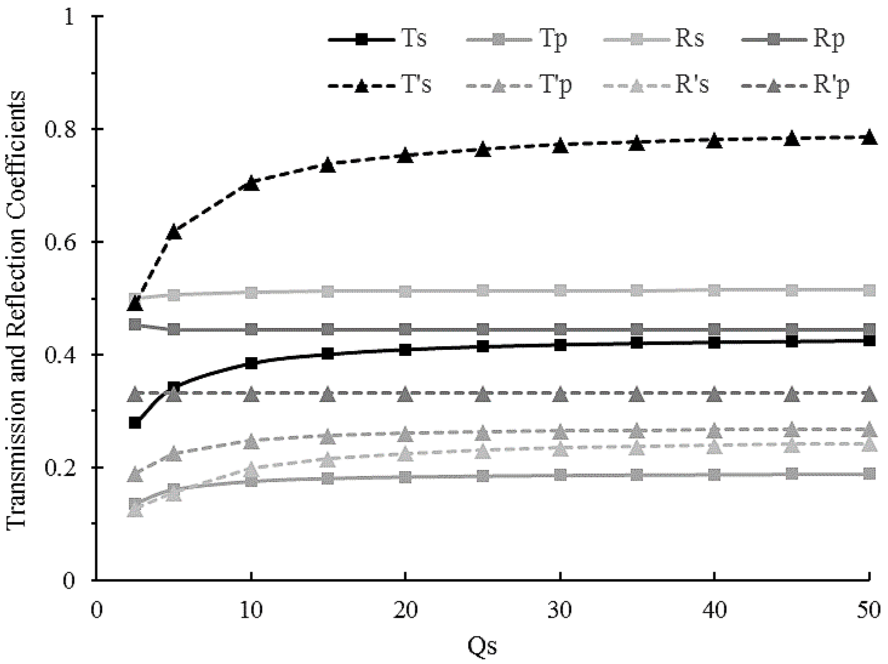

Fig. 23. Transmission and reflection coefficients with respect to quality factor (linearly elastic and nonlinear models).

Fig. 23 shows the comparative variations in transmission and reflection coefficients for the three-joint system of the present study for both the linearly elastic and nonlinear shear models. The coefficients indicated by prime symbols correspond to the linearly elastic shear model. It is evidently clear from Fig. 23 that over the range of 2.5-50 for the quality factor, the shear transmission coefficient has been noticeably reduced both in the linear (by as much as 60%) and more limitedly in the nonlinear model case (by as much as 39%), as depicted by T′s and Ts, respectively.

It is manifestly clear as well from Fig. 23 that for nonlinear shear model, Rp and Rs have both outstripped Ts for all ranges of quality factors. This indicates the effect of joint sliding on the reflection coefficients so that with the nonlinear shear model, wave energy is dissipated to a larger extent at the time of sliding and consequently, a greater portion of the incident wave energy is reflected back into the rock media. This is why for the same range of 2.5-50 of quality factor, Tp and Ts are consequently smaller than T′p and T′s, on average by ratios of 0.70 and 0.54, respectively. This is how nonlinear shear criterion affects the wave energy partitioning throughout the jointed rock mass media.

4.1.3 Special cases for viscoelastic saturated Shameshak Sandstone

In order to investigate the influencing factors on the results in the present study in a distinctive manner, the three-joint system is considered in the same previous conditions, except that the nonlinear shear model is assigned to only one of the joints. Additionally, only the variation in the shear transmission coefficient, i.e., Ts, is monitored and analyzed in all cases, for simplicity.

4.1.3.1 Effect of initial static shear strength of the joint

Fig. 24 shows the results on the basis that the nonlinear shear model is attributed to only joint 2, whereas in Fig. 25, the model has been applied for only joint 3. As it is evident, the initial static shear strength of the joints has a significant effect on the shear transmission coefficient in both cases (by as much as 38%, on average). It is clear that for a certain static shear strength, the variation in the records is more pronounced for the case of joint 2 as compared to the joint 3. This is because for joint 3, the effect of viscosity is correlated to the whole media between the three joints (the maximum allowable transmitting wave energy is limited to a certain amount by the sliding criterion no matter how much viscous the rock media along the propagation path is). While for joint 2, it is only the media between joints 1 and 2 that is limited by the slipping criterion across the joint. Consequently, the variation in the results is more palpable for joint 2 as compared to joint 3. This is yet another concrete proof on the reliability and validity of the results in the present paper.

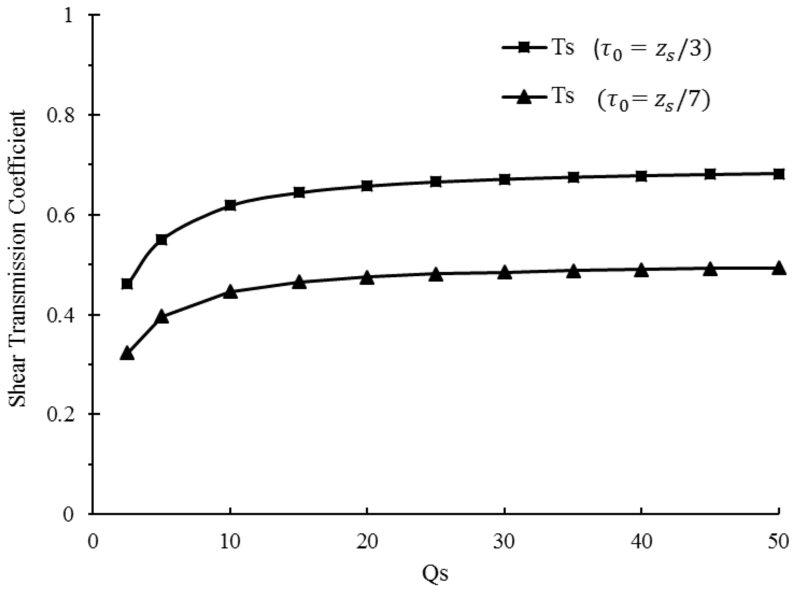

Fig. 24. Shear transmission coefficient in two different static shear strengths of the joint (nonlinear shear model assigned to only joint 2).

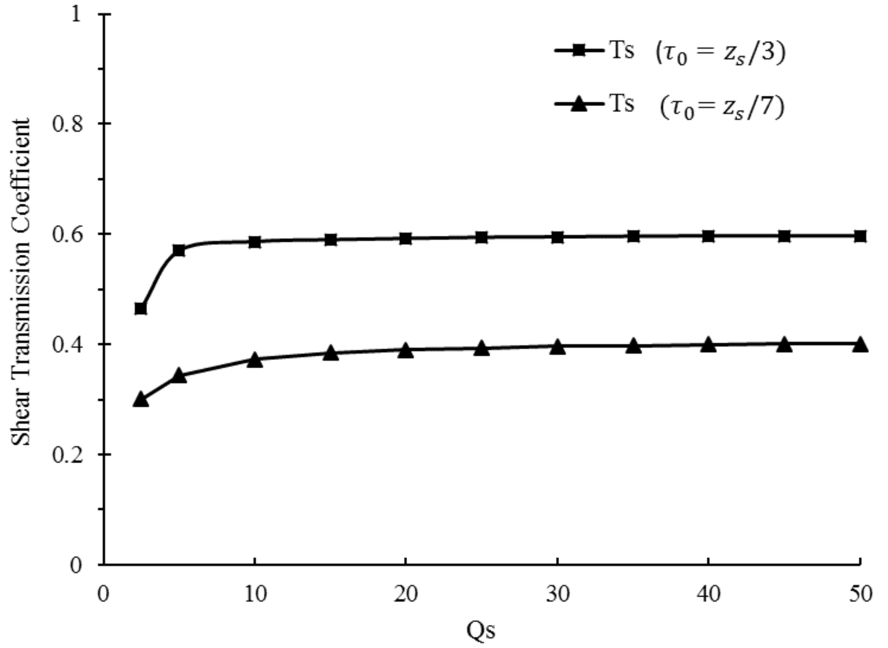

Fig. 25. Shear transmission coefficient in two different static shear strengths of the joint (nonlinear shear model assigned to only joint 3).

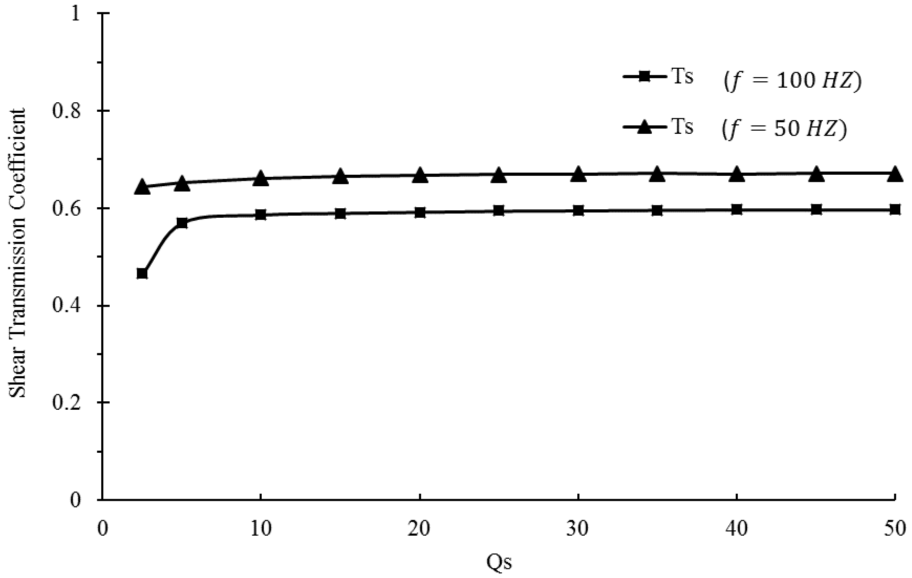

Fig. 26. Shear transmission coefficient in two different wave frequencies (nonlinear shear model assigned only to joint 3, $\tau_0 = z_s/3$).

4.1.3.2 Effect of wave frequency

In order to evaluate the effect of wave frequency on the shear transmission coefficient of the three-joint system over a range of quality factors, nonlinear shear model is only assigned to joint 3 so that the influence of viscosity could be recorded more obviously. The results are shown in Fig. 26 in which it is obvious that with the change in wave frequency from 100 to 50, the shear transmission coefficient is affected by as much as 14% for over the range of 2.5-50 for Qs. It should be noted that the discrepancy is primarily caused by the difference in the dynamic normal stress on the joint in the two wave frequencies.

4.1.3.3 Effect of joint spacing

In this section and for all cases, the

nonlinear shear model is only assigned to joint 3 ($\tau_0 = z_s/7$) and the results for the shear transmission coefficient are derived for two different sets of joint spacing and then are compared with those from the linearly elastic shear model. In addition, and as illustrated in Fig. 3, the joint spacing between joints 1 and 2, i.e. S_1 remains constant and the same as in previous sections, while the spacing for joints 2 and 3, i.e. S_2 changes.

Accordingly, four different cases are considered so that cases A and B represent the results of the nonlinear shear model for $S_2 = 10S_1$ and $S_2 = S_1$, respectively, while cases C and D demonstrate the results of the linearly elastic model in the same joint spacing sets, respectively. Fig. 27 shows the results for the shear transmission coefficient over a range of quality factors in all four cases, comparatively.

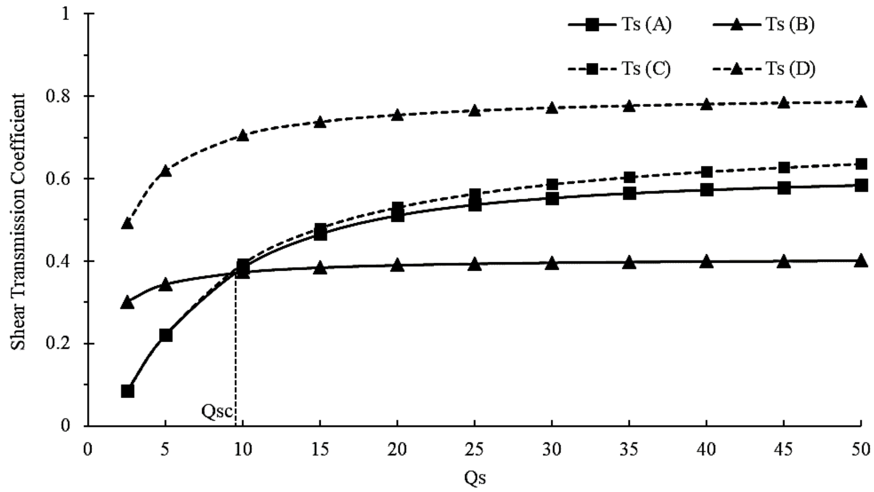

Fig. 27. Shear transmission coefficient in four different cases, A, B, C and D for joint 3.

As shown in Fig. 27, it is obvious that the greatest divergence between C and D occurs at the highest values of media viscosity. Whereas the two curves tend to converge as the quality factor approaches infinity, where the influence of viscosity totally disappears and the joint spacing no longer exerts any effect on the results.

Noticeably, this also indicates a substantive proof on the consistency and reliability of the results in the present study. Moreover, the substantial influence of sliding across joint 3 is clearly evident by comparing the curves B and D, where the wide discrepancy between the values of shear transmission coefficients on the two curves (the area between curves B and D in Fig. 27) arises exclusively from the incorporation of the nonlinear shear model. This is while the same mechanism in the higher joint spacing cases, i.e., A and C, causes much smaller difference in the values of shear transmission coefficient as the quality factor increases (the area between curves A and C in Fig. 27). It is obvious that the two curves A and C coincide as the quality factor approaches zero, as shown in Fig. 27. This could be yet another concrete consistency in the results of the developed TDRM in the present study.

Additionally, to interpret the discrepancy between A and B, a critical quality factor (Qsc as specified in Fig. 27) is defined as the intersection of the two curves. For the quality factors larger than Qsc where the media viscosity is relatively low, the difference in the values of shear transmission coefficient on the two graphs stems from the difference in the dynamic normal stress when slipping triggers across joint 3. In other words, because of the difference in the P wave and S wave speeds in the rock media ($C_p > C_s$), and because joint spacing, or the same stress wave propagation path, is 10 times greater in case A than that in case B ($S_2 = 10S_1$), the dynamic normal stress and consequently the dynamic shear strength of joint 3 (according to Coulomb shear criterion) will be higher in case A than in case B when the sliding criterion is satisfied across the joint. Therefore, higher values are obtained for shear transmission coefficient in case A as compared to case B. This is while for the quality factors lower than Qsc where the media viscosity is large enough as the dominant factor, the effect reverses back so that lower values for shear transmission coefficient are recorded for the case with the higher joint spacing (case A). This all represents as solid validation for the consistency and reliability of the results obtained in the present study.

In other words, the effect of joint spacing on the values of shear transmission coefficient should be analyzed and interpreted in tandem with the effect of media viscosity. That is why "dual" effect of joint spacing is introduced and discussed by means of critical quality factor (Qsc).

4.1.3.4 Effect of incidence angle (β)

In this section, the nonlinear shear model is assigned only to joint 3 and the variations in the shear transmission coefficient are investigated in two different joint spacing sets ($S_2 = S_1$ and $S_2 = 10S_1$) as well as two different incidence angles ($\beta = 20°$ and $\beta = 0$). The initial static shear strength is also considered to be $z_s/7$ in all cases. As it is shown in Fig. 28, for the case of normal incidence, the positive effect of joint spacing, as discussed in section 4.1.3.2, no longer exists so that it totally disappears in the normal incidence case with almost no divergence between the two graphs. This is because of the fact that in a normal incidence case, no P wave propagates towards joint 3 and consequently no dynamic normal stress is induced across the joint (according to Coulomb shear criterion). This causes the dynamic shear strength of the joint to remain constant over time, equaling the same initial static shear strength of the joint. Consequently, the maximum shear transmission coefficient is exclusively controlled by the static shear strength of the joint for any joint spacing and for any quality factor over which the sliding occurs across the joint, as evidenced in Fig. 28.

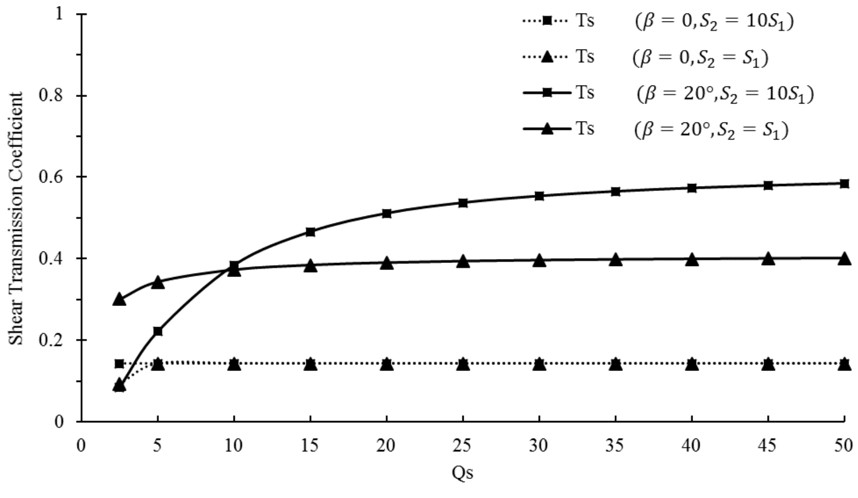

Fig. 28. Shear transmission coefficient in different incidence angles and joint spacing sets.

5 Conclusion

In the present study, based on the experimental data in two different air-dried and fully water-saturated conditions, a clay-rich rock called Shemshak sandstone was selected to represent the viscoelastic rock media for studying stress wave propagation in a three-joint system with an incident shear stress wave. In order to include the viscosity of the media, the Kelvin-Voigt model was adopted for the rock material and was incorporated into the time-domain recursive method (TDRM). Also, in order to include the sliding mechanism across the joints, a nonlinear shear model was adopted and incorporated into the analytical code so that the results were analyzed in comparison with those obtained from a linearly elastic shear model. The results can be described as follows:

1. Based on the well-known attenuative as well as time-delay effects, media viscosity exerts a significant influence particularly on the shear transmission coefficient in the case of an incident shear stress wave (by as much as 60% in linear shear model). This is while the effectiveness is mitigated in the case of nonlinear shear model (by as much as 39%) due to the restraining effect of the sliding model on the maximum dynamic shear stress across the joints (according to Coulomb criterion). Also, the viscosity effect is more pronounced on the shear transmission coefficient when the slipping model is assigned to joint 2 than joint 3 because of the wave propagation path involved. Plus, the oscillations in the wave graphs caused by multiple reflections (or the same secondary incident waves) are significantly attenuated in the higher values of viscosity.

2. The developed code in the present study, which is based on the TDRM method, is shown to successfully monitor and predict the slipping conditions under the nonlinear shear model. When the joints satisfy the slipping criterion in the nonlinear shear model, the maximum transmitted shear stress remains constant and equal to the dynamic residual shear strength of the joint. Additionally, a relatively higher portion of the incident shear stress wave is reflected to the media in the form of P and S reflected waves. Consequently, the shear transmission coefficient is remarkably reduced (from 60% to 39%, on average) as a result of sliding across the joints, whereas a significant enhancement is induced in the both P and S reflection coefficients. The effect of the slipping mechanism is potentially minimized with the increase of media viscosity as a direct consequence of wave attenuation so that wave energy is dissipated along the stress wave propagation path with the slipping criterion less likely to be satisfied.

3. The initial static shear strength of the joints has a significant effect on the shear transmission coefficient (by as much as 38% in the present analysis), so that it is especially emboldened in the case of normal incidence angle. This is due to the fact that in normal incidence, the dynamic shear strength only arises from the static shear strength where no dynamic normal stress is induced across the joint. This is why in a normal incidence case, the maximum shear transmission is exclusively determined by the static shear strength for any joint spacing and for any quality factor. In other words, the shear transmission coefficient reaches to maximum at a specific viscosity where the sliding starts to occur, so that it remains constant for any larger quality factors.

4. The effect of wave frequency on the shear transmission coefficient is primarily caused by the difference in the dynamic normal stress induced in the slipping joint, so that the shear transmission coefficient is relatively higher in lower frequencies (14% higher in 50 HZ than 100 HZ).

5. The effect of the slipping criterion on the shear transmission coefficient is highly correlated to the joint spacing at the same quality factor, in such a way that for larger joint spacing, the effect is enhanced at the higher values of quality factor. This is because at relatively higher joint spacing, the sliding criterion is satisfied at larger values of dynamic shear strength due to

the more pronounced difference in the arriving times of P and S waves on the joint interface. This mechanism allows the nonlinear shear model to gain higher dynamic normal stress before sliding starts across the joint, leading to a stronger shear transmission coefficient. This significant positive effect of joint spacing is reduced to zero for the normal incidence angle, where the dynamic shear strength only arises from the initial static shear strength of the joint.

Acknowledgement
The author would like to express his sincere gratitude to Noavaran Sang Arya company, managed by Mrs. Saeedeh Rasouli Jazi, for providing financial and logistical support which contributed to the successful completion of this research.

Author contributions
AN: Investigation, Software, Formal Analysis, Visualization, Methodology, Validation; KG: Resources, Supervision; RN: Resources, Supervision

References
Bedford, A. and D. Drumheller, "*Introduction to Elastic Wave Propagation, 1994"*. ed: John Wiley and Sons, New York. 1994

Best, A.I.," *Seismic attenuation and pore-fluid viscosity in Clay-rich sandstones"*, in *SEG Technical Program Expanded Abstracts 1992*. Society of Exploration Geophysicists. p. 674–676. 1992

Bieniawski, Z. and M. Bernede." *Suggested methods for determining the uniaxial compressive strength and deformability of rock materials: Part 1. Suggested method for determining deformability of rock materials in uniaxial compression"*. in *International journal of rock mechanics and mining sciences & geomechanics abstracts*. Elsevier.1979

Carcione, J.M.," *Wave fields in real media: Wave propagation in anisotropic, anelastic, porous and electromagnetic media"*. Vol. 38. Elsevier.2007

Carcione, J.M., F. Poletto, and D. Gei, "*3-D wave simulation in anelastic media using the Kelvin–Voigt constitutive equation"*. Journal of Computational Physics. **196**(1): p. 282–297. 2004

Chai, S., et al., "*Theoretical study for induced seismic wave propagation across rock masses during underground exploitation"*. Geomechanics and Geophysics for Geo-Energy and Geo-Resources. **3**(2): p. 95–105. 2017

Chai, S., et al., "*Stress wave propagation across a rock mass with two non-parallel joints"*. Rock Mechanics and Rock Engineering. **49**(10): p. 4023–4032. 2016

Chen, C.-S., E. Pan, and B. Amadei, "*Determination of deformability and tensile strength of anisotropic rock using Brazilian tests"*. International Journal of Rock Mechanics and Mining Sciences. **35**(1): p. 43–61. 1998

Hu, Y., X. Wang, and Z. Zhong, "*Investigations on the jointed influences of saturation and roughness on the shear properties of artificial rock joints"*. Geomechanics and Geophysics for Geo-Energy and Geo-Resources. **8**(4): p. 115. 2022

Huang, X., et al., "*Stress wave propagation through viscous-elastic jointed rock masses using propagator matrix method (PMM)"*. Geophysical Journal International. **200**(1): p. 452–470. 2014

Huang, X., et al., "*Stress wave propagation through rock joints filled with viscoelastic medium considering different water contents"*. Applied Sciences. **10**(14): p. 4797. 2020

Li, H., et al., "*Influence of water saturation time on microstructure and mechanical properties of jointed limestone"*. Frontiers in Earth Science. **10**: p. 922683. 2022

Li, J., et al., "*A time-domain recursive method to analyse transient wave propagation across rock joints"*. Geophysical Journal International. **188**(2): p. 631–644. 2012

Li, J., et al., "*Analytical study of ground motion caused by seismic wave propagation across faulted rock masses"*. International journal for numerical and analytical methods in geomechanics. **42**(1): p. 95–109. 2018

Li, J. and G. Ma, "*Analysis of blast wave interaction with a rock joint"*. Rock Mechanics and Rock Engineering. **43**(6): p. 777–787. 2010

Li, J., G. Ma, and J. Zhao, "*Stress wave interaction with a nonlinear and slippery rock joint"*. International Journal of Rock Mechanics and Mining Sciences. **48**(3): p. 493–500. 2011

Rocks, S.," *Petrology of sedimentary rocks"*. Springer.1968

Schoenberg, M., "*Elastic wave behavior across linear slip interfaces"*. The Journal of the Acoustical Society of America. **68**(5): p. 1516–1521. 1980

Xu, J., et al., "*Evaluation of the water weakening coefficient of sandstones by using non-*

destructive physical parameters". Frontiers in Earth Science. **12**: p. 1460912. 2024

Yang, H., et al., "*Water effects on elastic S-wave propagation and attenuation across single clay-rich rock fractures: insights from ultrasonic measurements".* Rock Mechanics and Rock Engineering. **57**(4): p. 2645–2659. 2024

Yin, H., et al., "*Fluid substitution and shear weakening in clay-bearing sandstone at seismic frequencies".* Journal of Geophysical Research: Solid Earth. **124**(2): p. 1254–1272. 2019

Zhao, J. and J. Cai, "*Transmission of elastic P-waves across single fractures with a nonlinear normal deformational behavior".* Rock Mechanics and Rock Engineering. **34**(1): p. 3–22. 2001

Zheng, L. and Q. Zuo, "*Experimental study on the effect of water-induced deterioration on shear properties of bolted rock joints".* Case Studies in Construction Materials. **20**: p. e03027. 2024.